A Miniature Physical Simulator for Pilgering

Jaiveer Singh[1], S. Mahesh[2,*], Shomic Roy[1,3], Gulshan Kumar[1], D. Srivastava[4], G. K. Dey[4], N. Saibaba[5] and I. Samajdar[1]

[1]Department of Metallurgical Engineering & Materials Science, Indian Institute of Technology Bombay, Powai, Mumbai-400 076, India

[2]Department of Aerospace Engineering, Indian Institute of Technology Madras, Chennai-600 036, India

[3]Scientific Services, Tata Steel Limited, Jamshedpur-831 001, India

[4]Materials Science Division, Bhabha Atomic Research Centre, Trombay, Mumbai-400 085, India

[5]Nuclear Fuel Complex, Hyderabad-500 062, India

*Corresponding author: smahesh@iitm.ac.in (S. Mahesh)

Abstract:

Pilgering is a complex incremental manufacturing process for seamless tubes. In this work, a miniature physical simulator for pilgering was designed and fabricated. This miniature simulator employs a grooved roll-die and a mandrel and can impose controlled reductions in both tube diameter and wall thickness. Pilgering deformation over a range of ratios of reductions in wall thickness and in tube diameter, known as the Q-factor, was imposed on hemi-cylindrical zirconium alloy specimens. The influence of the Q-factor on the microstructure and deformation texture of the deformed specimens was quantified. A polycrystal plasticity calculation based on the binary tree model was used to simulate texture evolution during the simulated pilgering process. The computer model quantitatively captured the variation with Q of the Kearns factors, as measured in the physically simulated specimen. The small differences noticed between the predicted and experimental final textures point to unaccounted transverse components of the flow field. These observations suggest that physical and/or computer simulations can form the basis of a rapid methodology for tool selection to realize prescribed post-pilgering textures.

Keywords: Zirconium, Pilgering, Plastic Deformation, Texture, Microstructure.

1. Introduction

a. Tube forming by pilgering

Pilgering is an incremental compression forming process, which involves repeated rolling of a tubular job over a mandrel using a roll-die with a tapered groove (Figure 1(a)). Combinations of forward and return strokes plus appropriate rotations about the tube axis ensure manufacturing with precise dimensional tolerances. As described in detail by Verlinden et al. (2007), the pilgering process involves 'biting' followed by forging, polishing and then idling in a single pilgering stroke. The tapered groove on the roll-die allows variation of the imposed deformation with axial position during a stroke. Cold pilgering yields very high reductions even in difficult to form materials. The nuclear industry has used pilgering for the fabrication of seamless zirconium (Zr) tubes. Processing routes involving alternating pilgering and heat-treatment steps, to produce thin walled tubes for fuel clads, have been described by Saibaba (2008). This work emphasizes the determination of a processing route to fabricate the tube product that meets service requirements; the relationship between processing route and tube properties was not systematically studied.

The roll-die/mandrel tooling lies at the core of pilgering technology, as it determines the productivity and dimensional control over the processed tube. The effect of the tooling geometry on important macroscopic properties such as surface roughness, propensity for oxidation, and formability, has been investigated in the literature. For example, Aubin et al. (1994) correlated the incidence of surface defects to tool design and rolling parameters. Abe and Furugen (2012) made an important contribution to formability assessment during pilgering. They related the critical strain to inner wall fissuring during pilgering to the strain at failure developed in an equivalent compression specimen aligned with the circumferential direction. These process-property relationship characterizations were limited to the macroscopic scale, and did not provide a microstructural explanation. The relationship between the surface roughness and oxidation rate of the tube surface was investigated by Akhiani and Szpunar (2013). In addition to obtaining macroscopic characterizations, these authors also established a micostructural relation between the orientation of the monoclinic oxide grains, and the h.c.p. Zr.

b. Crystallographic texture

An important characteristic of a pilgered Zr tube, which determines its suitability for nuclear applications is its crystallographic texture. Again, the development of the crystallographic texture is determined by the tooling. The crystallographic texture affects in-service behavior such as creep-rate and irradiation swelling, as summarized in the review by Tenckhoff (1988). The crystallographic texture also determines the orientation of hydride precipitates, which are potential locations of brittle crack initiation. The crystallographic texture, and hydride precipitate orientation were correlated by Shinohara et al. (2009) and Vaibhaw et al. (2008). The latter authors also established a correlation with in-reactor performance of the pilgered tubes. Internal stresses developed in the pilgered tube and the crystallographic texture were related by Gurao et al. (2014). In summary, a strong correlation between both microscopic and macroscopic tube properties and crystallographic texture has been established by these works. This suggests that process design to enhance material properties of the tube product will require a good understanding of the relationship between tooling, and the final crystallographic texture.

Producing a number of geometric variants of the tooling in order to establish the relationship between tool geometry on the one hand, and material flow, and crystallographic texture development, on the other, is not usually feasible in a full-scale pilgering mill, due to material, time and cost constraints. Therefore, attempts have been made to understand texture development through polycrystal plasticity simulations. Lebensohn et al. (1996) and Girard et al. (2001) used the viscoplastic self-consistent (VPSC) polycrystal plasticity model to predict the final texture after pilgering. They could obtain qualitative comparisons between computer simulated and experimental textures after multiple pilgering passes. More recently, some of the present authors (Singh et al. (2015a)) used a binary tree based polycrystal model to predict texture evolution during pilgering. They too obtained only qualitative agreement with textures measured in a partially pilgered tube.

A commonality between these modelling works is the deformation history imposed: all works assume that the material flow during pilgering is akin to monotonic flow through a convergent channel. In Girard et al. (2001), and Singh et al. (2015a), an additional uniform shear

component, representing frictional interactions between tube and tooling was superposed over the monotonic flow. The assumed deformation history in the computer simulations is in stark contrast with the full-scale process, wherein non-monotonic time-varying normal and frictional contact forces are applied.

The reason for the quantitative deviation between the texture measured in a pilgered tube and that predicted by computer simulations is not presently clear. One obvious possibility is that the deviation is because the deformation history imposed upon the computer material is unrealistically idealized. A second possibility is that the computer simulations may be missing important microscopic phenomena occurring in the physical material, which help accommodate the imposed plastic deformation, in a way not captured by the computer simulation.

c. Physical simulation of pilgering

Physical simulations of properties and microstructures are an important aspect of complex forming and thermomechanical processing. For example, deformation simulators have been successfully used to optimize roll-pass schedules by Abe et al. (2000). As another example, the bulge test for laboratory forming limit diagrams provides important inputs to more complex sheet metal forming, as in Hwang et al. (2009). This context naturally suggests a miniature physical simulator for pilgering. Such a physical simulator will enable the examination of many more tool geometry variants than would be possible in a full-scale pilgering mill, on account of the much lower associated material, time and cost requirements. The physical simulator will also permit more control over the imposed tube deformation than a full-scale mill. The present authors are unaware of any studies of pilgering based on physical simulation, reported in the literature.

In this study, a physical simulator for pilgering capable of imposing controlled monotonic deformations is designed, fabricated and used to study the variation of final microstructure and texture with tooling geometry. The tooling geometry is parameterized by a standard scalar process variable namely, the Q-factor, due to Abe et al. (1994). The monotonic loading pattern of the simulated pilgering process is compared with the texture predictions obtained from a binary-tree based polycrystal plasticity model, proposed by Mahesh (2009).

During physical simulations, a controlled monotonic deformation is applied to the specimen. A key finding of the present study is that the crystallographic texture after physically simulated pilgering agrees quantitatively with that obtained from computer simulations. This suggests that the micro-mechanisms of plastic deformation are accurately captured in the present model. This also implies that improving the accuracy of the imposed deformation history in computer simulations of full-scale pilgering will improve their predictive accuracy.

This article begins with a description of the material point deformations in pilgering idealized as flow through a convergent channel, and in channel die compression idealized as plane strain deformation in Sec. 2. This is followed in Sec. 3 by a description of the physical pilgering simulator, and the experimental and computational procedures adopted for studying microstructure and texture evolution with Q. A comparison of the experimental and computer model predicted textures for different Q appears in Sec. 4. It will be shown that the texture variation with Q-factor in the physical simulations, described in terms of the Kearns factors, is captured quantitatively by the computer simulation. Consequences of this result are discussed in Sec. 5.

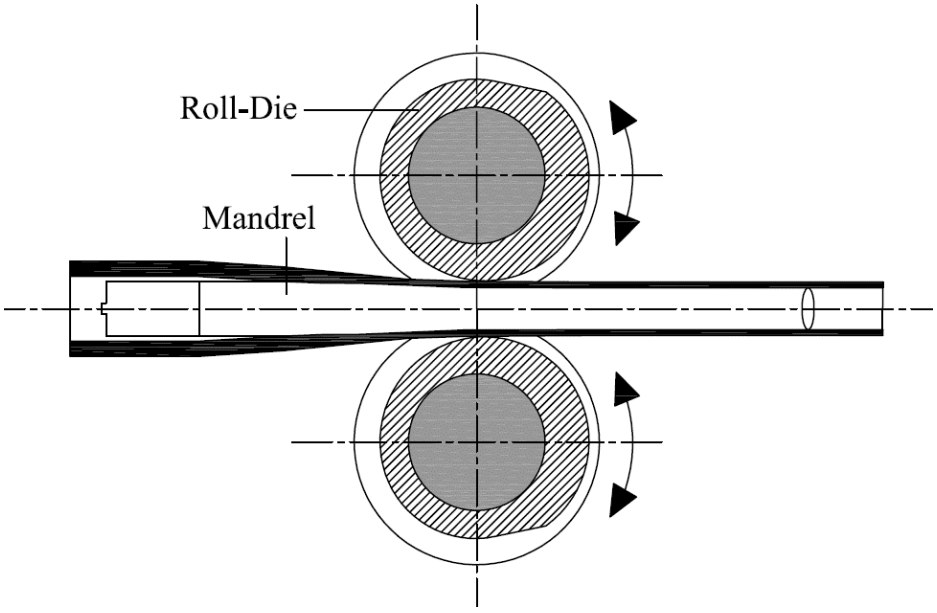

(a)

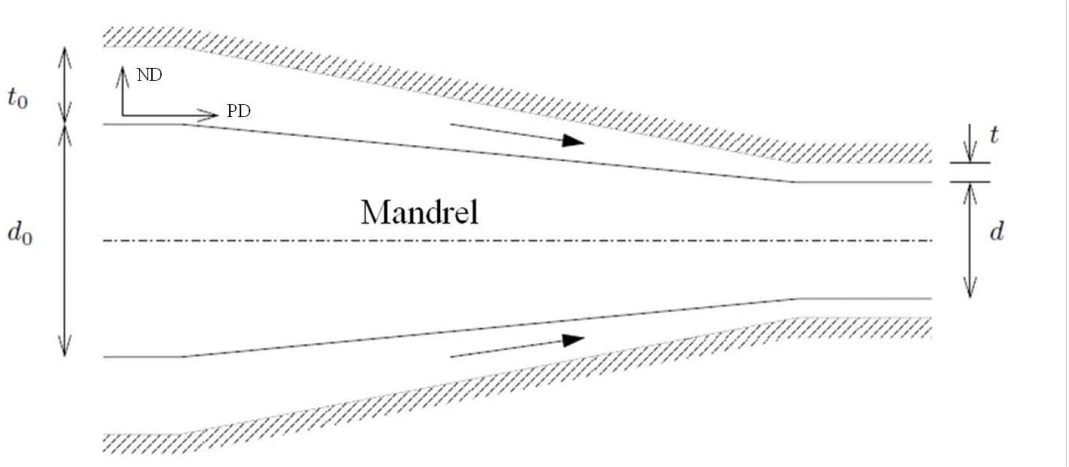

(b)

Figure 1: Schematic of the (a) pilgering process and (b) flow through a convergent channel. (a) highlights the grooved roll-die and the mandrel: tools important for the physical simulator. (b) was used in an earlier study by Gurao et al. (2014) and Singh et al. (2015a), as well as in the present manuscript, for modeling the texture developments during pilgering. In (b), pilgering (PD) and normal directions (ND) are shown. Also indicated are the initial and final tube diameters (d_0 and d) and wall thicknesses (t_0 and t).

2. Kinematics of Pilgering and Channel Die Compression

The Q-factor is the ratio between reductions in wall thickness and the diameter, as defined by Abe et al. (1994). For $Q > 1$ the reduction in wall thickness dominates, while $Q < 1$ deformation implies larger reductions in the tube diameter. As noted by Allen et al. (2005) the basal poles in zirconium alloys align themselves in the direction of the major compressive strains. This observation has been reaffirmed by the later texture measurements of Choi and Inoue (2010). This implies that the Q-factor plays a key role in the development of texture/microstructure. For example, $Q < 1$ is expected to cause compressive forces in the tangential direction and a preferential alignment of the basal poles in that direction, as discussed by Tenckhoff (2005).

The simulator was designed to explore the role of Q-factor on texture and microstructure developments. With respect to engineering strains, the Q-factor has been defined following Murty and Charit (2006) as:

$$Q_{eng} = \left(\frac{\Delta t/t_0}{\Delta d/d_0}\right), \tag{1}$$

where, t_0 is the initial tube thickness, Δt is the reduction in tube thickness, d_0 is the initial tube diameter, and Δd is the reduction in tube diameter. Q_{eng} is the ratio of respective reductions in tube thickness and in tube diameter. Alternatively, the Q-factor can also be defined with respect to true strains, following Abe et al. (1994):

$$Q_{true} = \left(\frac{\ln(t/t_0)}{\ln(d/d_0)}\right), \tag{2}$$

where, initial and final tube diameters and wall thicknesses are d_0, d, t_0 and t, respectively.

Five mandrels were fabricated for this study to generate five different Q-factors. The initial and final diameters for the tube specimens and corresponding wall thicknesses are given in Table 1. Both Q_{eng} and Q_{true} corresponding to these mandrels are listed in Table 2. Q_{eng} and Q_{true} are seen to be only marginally different in all cases. As Q_{true} more accurately captures the imposed large deformations on the specimen, Q_{true} will henceforth be referred to as the Q-factor.

Table 1: Initial and final tube wall thicknesses and diameters of the five specimens studied.

Mandrel	Tube Wall Thickness (in mm)		Tube Diameter (in mm)	
	Initial (t_0)	Final (t)	Initial (d_0)	Final (d)
1	1	0.94	8.2	7.77
2	1.4	1.29	7.6	7.24
3	1.675	1.535	7.325	7.075
4	1.925	1.735	7.075	6.915
5	1.75	1.52	7.25	7.18

Table 2: Q-factors, final effective strain $(\bar{\varepsilon})$ and deviation (θ) for the five specimens. The Q-factors were calculated as both Q_{eng} (Eq. (1)) and Q_{true} (Eq. (2)), final effective strain $(\bar{\varepsilon})$ (Eq. (11)) and deviation (θ) (Eq. (7)).

Mandrel	Q_{eng}- Factor	Q_{true}- Factor	Final Effective Strain $(\bar{\varepsilon})$	Deviation (θ) $\theta = \frac{1+2Q}{2\sqrt{1+Q+Q^2}}$
1	1.14	1.15	0.116	0.885
2	1.65	1.69	0.188	0.929
3	2.44	2.51	0.217	0.961
4	4.36	4.54	0.274	0.985
5	13.6	14.5	0.313	0.998

The deformation history imposed on the specimen is typically described by Kocks et al. (1998) in terms of the velocity gradient, $L_{ij} = \partial v_i/\partial x_j$, where v_i denotes the components of material point velocity at spatial coordinate x_j. During industrial pilgering, material points are subjected to complex non-monotonic deformation histories, as shown by Furugen and Hayashi (1984). Nevertheless, for the purpose of capturing the qualitative evolution of deformation texture, Lebensohn et al. (1996), Girard et al. (2001) and Singh et al. (2015a) have found it adequate to represent metal flow during pilgering as that of flow through a convergent channel.

The same flow field is also applied in the present work, and accordingly, the velocity gradient is taken to be

$$L_{[PD-TD-ND]} = \begin{bmatrix} 1+Q & 0 & 0 \\ 0 & -1 & 0 \\ 0 & 0 & -Q \end{bmatrix}. \tag{3}$$

In studying the variation of crystallographic texture with Q, it will be useful to compare with the velocity gradient of plane strain compression, $L^{PSC}_{[PD-TD-ND]}$,

$$L^{PSC}_{[PD-TD-ND]} = \begin{bmatrix} 1 & 0 & 0 \\ 0 & 0 & 0 \\ 0 & 0 & -1 \end{bmatrix}. \tag{4}$$

Following Schmitt et al. (1985) and Peeters et al. (2001), let the strain mode be defined as the ratio of the velocity gradient normalized by its Eucledian norm. Thus, the strain mode for pilgering is given as

$$S_{[PD-TD-ND]} = L_{[PD-TD-ND]}/\sqrt{2(1+Q+Q^2)}\,. \tag{5}$$

For plane strain compression, similarly, the strain-mode is

$$S^{PSC}_{[PD-TD-ND]} = L^{PSC}_{[PD-TD-ND]}/\sqrt{2}. \tag{6}$$

Eqs. (3)-(6) imply that $S_{[PD-TD-ND]}$ approaches $S^{PSC}_{[PD-TD-ND]}$ as $Q \to \infty$. It will also prove useful in the sequel to define a quantitative measure of the deviation between the strain modes, $S_{[PD-TD-ND]}$ and $S^{PSC}_{[PD-TD-ND]}$. Again following Schmitt et al. (1985), this deviation is quantified by the scalar

$$\theta = S_{[PD-TD-ND]} : S^{PSC}_{[PD-TD-ND]} = \frac{1+2Q}{2\sqrt{1+Q+Q^2}}. \tag{7}$$

Eq. (7), applied to the five mandrels studies yields the θ listed in Table 2.

The velocity gradients of Eq. (3) and Eq. (4) are symmetric. Therefore, they also represent the strain-rates $D_{[PD-TD-ND]}$ and $D^{PSC}_{[PD-TD-ND]}$, as given by Kocks et al. (1998). The equivalent or von Mises strain-rate is given by $\overline{D} = \sqrt{\left(\frac{2}{3}\right) D : D}$, where : denotes the tensor dot. Accordingly,

the equivalent strain-rate corresponding to pilgering is given by

$$\overline{D} = \sqrt{\left(\frac{4}{3}\right)(1 + Q + Q^2)}, \tag{8}$$

while that corresponding to plane strain compression is the more familiar

$$\overline{D}^{PSC} = \sqrt{\left(\frac{4}{3}\right)}. \tag{9}$$

Let F denote the deformation gradient of a material point. Its evolution with time then follows Kocks et al. (1998) $\dot{F} = LF$. If the velocity gradient L were assumed constant through the deformation, as in the present instance, the evolution equation can be integrated in closed form to obtain $F = F_0 \exp(L\Delta t)$, where F_0 denotes the initial deformation gradient at time $t = 0$ and F denotes the deformation gradient at time $t = \Delta t$. Identifying the initial deformation gradient with the identity, and taking L to be that given by Eq. (3), we have

$$F_{[PD-TD-ND]} = \exp\left(\begin{bmatrix} 1+Q & 0 & 0 \\ 0 & -1 & 0 \\ 0 & 0 & -Q \end{bmatrix}\Delta t\right). \tag{10}$$

In Eq. (10), exp denotes the matrix exponential. The thickness reduction factor (ratio of thickness reduction and initial thickness) along the ND direction is $r = 1 - F_{ND,ND} = 1 - \exp(-Q\Delta t)$. This gives a simple relation between r and time of deformation Δt following Eq. (3): $\Delta t = -\frac{\ln(1-r)}{Q}$. The corresponding relationship for the plane strain compression case is $\Delta t = -\ln(1-r)$.

Let the von Mises strain be denoted by $\bar{\varepsilon}$. Then, $\bar{\varepsilon} = \overline{D}\Delta t$, and the relation between the von Mises strain and thickness reduction r during pilgering is found to be

$$\bar{\varepsilon} = \overline{D}\Delta t = -\sqrt{\left(\frac{4}{3}\right)\frac{1+Q+Q^2}{Q^2}}\ln(1-r). \tag{11}$$

The corresponding expression for plane strain compression is $\bar{\varepsilon}^{PSC} = -\sqrt{\left(\frac{4}{3}\right)}\ln(1-r)$. The final effective strains listed in Table 2 are obtained from Eq. (11).

3. Experimental and Modeling Procedure

3.1. Physical Pilgering Simulator: Design and Fabrication

To generate the complex tri-axial strain-mode of the pilgering process as discussed by Furugen and Hayashi (1984), a miniature physical simulator was designed. The set-up consisted of grooved roll-die, mandrel and housing. Designed roll-die with semi-circular groove on the periphery of the roll and mandrel are shown in Figure 2(a) and 2(b), respectively. Both require a housing, where the roll-die plus shaft was placed in a commercial ball bearing and mandrel was held in an appropriate slot. In standard pilgering process (see Figure 1(a)), a continuous grooved roll of varying diameter rolls over a mandrel. The simulator, on the other hand, does not have a continuous groove. It also does not allow 'turnings' as used in the actual pilgering process, as described by Strehlau (2006). Though only one set of roll-die (maximum and minimum groove diameters of 8 and 5 mm respectively) was tested, it is apparent that different roll-die designs can be tested in the simulator easily. Engineering drawings (Figure 2(a) and Figure 2(b)) and actual photographs (Figure 2(c) and Figure 2(d)) are included in this manuscript. Standard tool steel was used to fabricate the simulator.

The pilgering physical simulations were carried out by placing an appropriately shaped sample (semi-circular tube) between the roll-die and mandrel, all held together by the housing, and then pushing the mandrel with a standard mechanical testing system. The specimens were moved incrementally to achieve the required von Misses effective strain (given in Table 2) in 1-2 passes for different Q-factors. The hemi-cylindrical tubes were 5 mm long, with wall thicknesses given in Table 1.

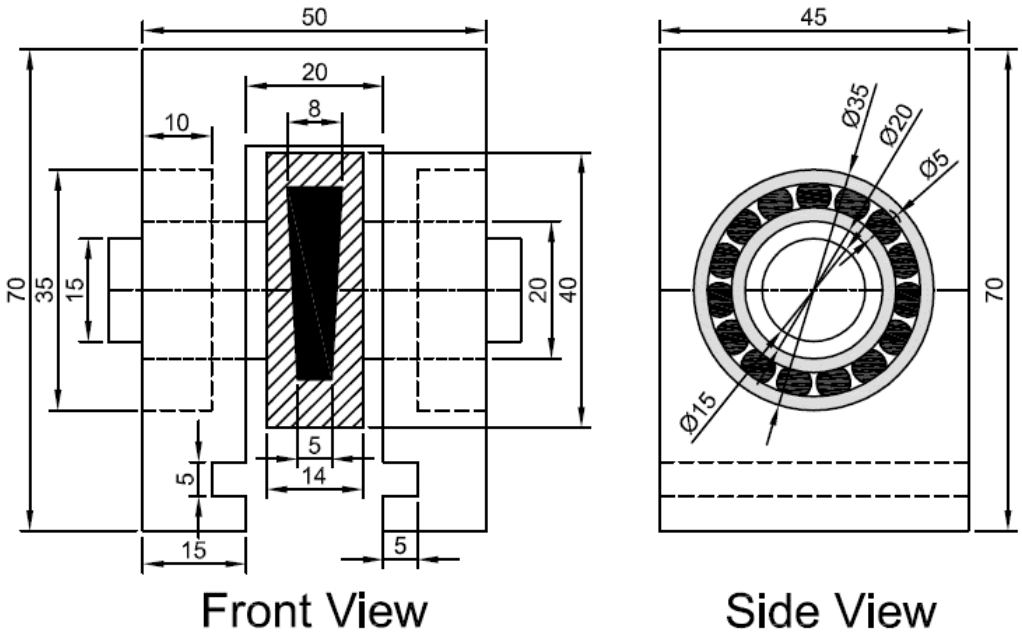

(a)

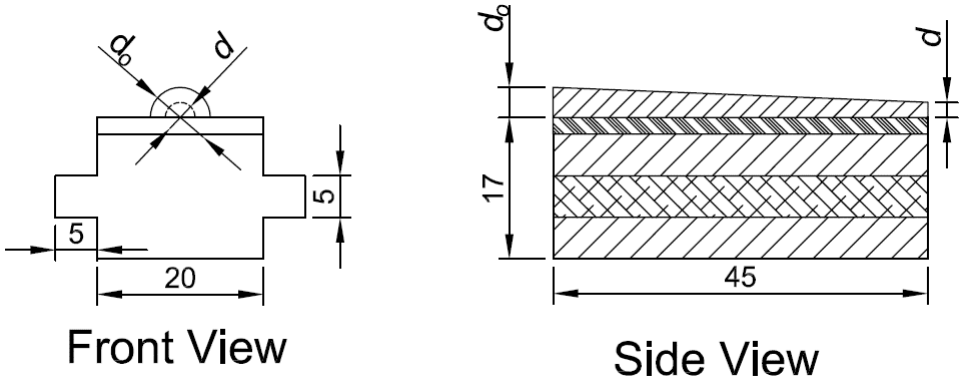

(b)

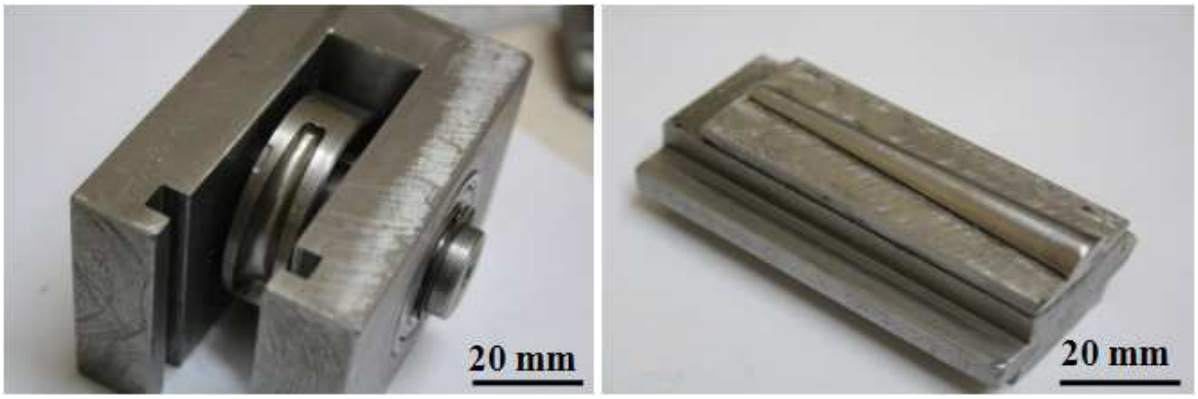

(c) **(d)**

Figure 2: Engineering drawings of the: (a) roll-die and (b) mandrel. Both front and side views are included. All dimensions in mm. Actual photographs of (c) roll-die (plus housing) and (d) mandrel.

3.2. Microstructural Characterization

The chemical composition of the Zircaloy-4 samples used in the present study is given in the Table 3. For microstructural characterization, samples were polished through standard metallography and electro-polishing following Krishna et al. (2006). All the microstructural measurements were made in the long transverse section, containing pilgering (PD) and normal (ND) directions. The EBSD (electron back-scattered diffraction) measurements were made on an EDAX-OIM^{TM} (orientation imaging microscopy) EBSD system in a FEI^{TM} Quanta 3D-FEG (field emission gun) SEM (scanning electron microscopy). In each sample, an area of 250μm x 300μm was covered at 0.2 μm step size. At least three scans were taken at each sample.

Table 3: Chemical composition of Zircaloy-4 used in this study.

Elements	Sn (wt. %)	Fe (wt.%)	Cr (wt.%)	Al (ppm)	Hf (ppm)	C (ppm)	Zr
	1.5	0.22	0.1	39.0	<50	<55	Balance

Incomplete ((0002), $(10\bar{1}0)$, $(10\bar{1}2)$, and $(10\bar{1}3)$) pole figures were measured on a PANalytical^{TM} X'Pert PRO MRD system for bulk texture measurements. A monochromatic Cu-K_α beam of 800 micron spot size was used. This was approximately 80% of the sample area. Bruker^{TM} D8 Discover system using micro-focus and area detector (Vantec^{TM}) was used for texture measurement at through thickness locations: near roll, center and near mandrel. A laser-tracker enabled identification of the exact identification. A 100 micron spot size, with 2 millimeter oscillation on pilgering direction, was used. Standard Schulz method in reflection mode described by Cullity and Stock (2001) was used for all pole figure measurements. Commercial software, LaboTex from LaboSoft^{TM}, was used to determine the ODFs using the Arbitrarily Defined Cells (ADC) Method developed by Raabe and Lücke (1993).

3.3. Modeling and Computer Simulation

Texture evolution was predicted using a computer code implementing a rate-independent binary tree based polycrystal plasticity model developed by Mahesh (2010). Given inputs of grains abutting each grain, grain lattice orientations, grain volume fractions, slip and twin systems that can be potentially activated, and their hardness evolution with grain deformation, this model predicts the mechanical response and texture evolution of the polycrystal. The first

three inputs are obtained from an EBSD micrograph. Grain volume fractions are assumed to be proportional to grain areas obtained from the micrograph. A binary tree representation of the EBSD micrograph is constructed following the approach detailed for texture evolution in Singh et al. (2015a). Key aspects of this representation are: (i) Each grain is divided into as many sub-domains as the number of its neighbors. Through this sub-division, each sub-domain is associated with a grain boundary facet of the original grain. (ii) Each sub-domain is assumed to deform homogeneously and compatibly with another sub-domain across the grain boundary facet. (iii) A pair of such sub-domains forms an ALAMEL unit in the terminology of Van Houtte et al. (2005), which deform with velocity and traction continuity with another ALAMEL unit. (iv) Larger and larger aggregates of such pairs are recursively formed, each of which deforms compatibly with another such aggregate. (v) The recursive pairing culminates at the root node of the binary tree, which represents the entire polycrystalline aggregate. The root node is required to deform following the imposed velocity gradient of Eq. (3) or Eq. (4).

An example of the binary tree representation of the microstructure is shown in Figure 3. An idealized part of a microstructure featuring a central grain surrounded by four grains is shown in Figure 3(a). The corresponding binary tree is shown in Figure 3(b). The 4-faceted central grain interacts with its neighbors across four planar grain boundaries. These interactions are modeled by sub-dividing the original grain into four sub-domains, A, B, C, and D, as shown. The sub-divisions of the neighboring grains abutting these four regions are labeled A1, B1, C1, and D1, respectively. Nodes labeled 1, 2, 3 and 4 represent ALAMEL units. Interactions across grain boundary facets between the constituent sub-domains are implemented enforced at the ALAMEL units. Longer range interactions, *e.g.*, that between regions A and B1 are also accounted for in the binary tree-based model, through the continuity conditions enforced between the sub-aggregate formed by regions A and A1 (termed 1 in Figure 3(b)) and that between the sub-aggregates formed by regions B and B1 (termed 2). Still longer range interactions are also captured, albeit more and more approximately, at higher levels of the binary tree.

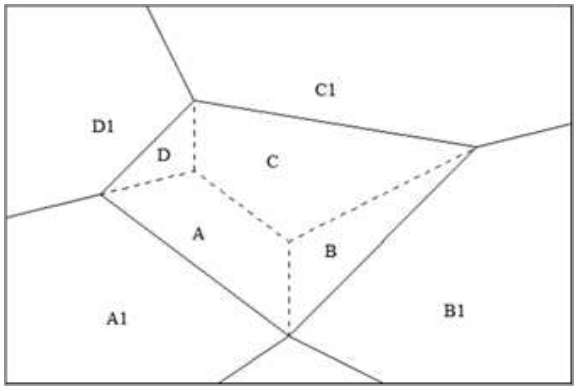

(a)

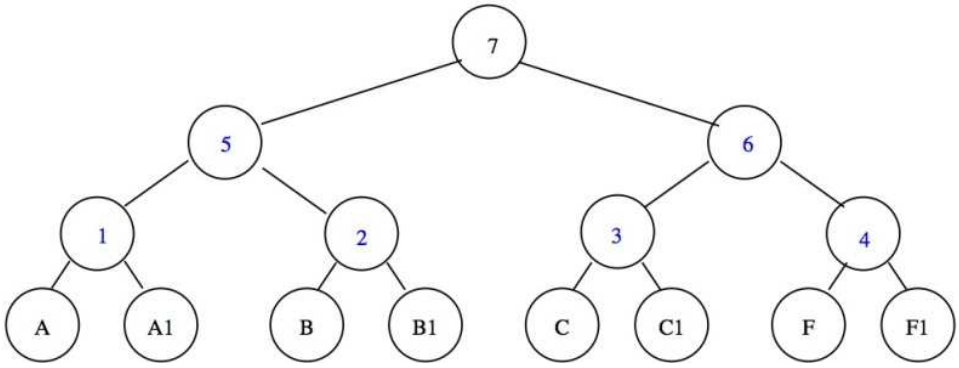

(b)

Figure 3: Binary tree based model (Mahesh (2009)) of a schematic idealized microstructure. (a) Idealized microstructure; (b) Balanced binary tree representation of (a).

Each of the $2^{12} = 4096$ sub-domains of grains in the present binary tree based model was obtained by area weighted random sampling from an EBSD micrograph of the undeformed specimen. The model hexagonal close packed (hcp) grains, and sub-domains, are assumed to have the following plastic deformation modes: prismatic slip $(1010)\langle 1120\rangle$, pyramidal slip $\{1011\}\langle 1123\rangle$, and extension twinning $\{1012\}\langle 1011\rangle$ following e.g., Tenckhoff (1988) and Tomé et al. (2001). As is common in the literature, e.g., Kocks et al. (1998), Schmid's law is taken to govern the activation of all slip and twinning systems. For simplicity, both slip and twinning systems are assumed to be non-hardening. The constant critical resolved shear stress of the prismatic slip systems, pyramidal slip systems and extension twinning systems are taken to be 45 MPa, 135 MPa, and 55 MPa, respectively. Note that these absolute values are not particularly relevant, only the relative values (ratios) are meaningful.

Activation of twinning systems and accommodation of shear by their activation entails a transformation of the lattice orientation of the sub-domain, as described by Christian and Mahajan (1995). Let γ_t denote the accumulated shear in twinning system t. Let the characteristic twinning shear be Γ_t. Then, the twin volume fraction is given by

$$f_t = \gamma_t / \Gamma_t. \tag{12}$$

In zirconium, $\Gamma_t = 0.169$ for the six $\{1012\}\langle 1011\rangle$ extension twinning systems. Twin growth in the model is reflected in an increasing f_t. Also, if the volume fraction of twin variant t exceeds a pre-set threshold ($f_t \geq f_0 = 0.8$), the lattice orientation of the entire parent sub-domain is completely reoriented to that of twin variant t.

4. Results and Discussion

4.1. Microstructure

Figure 4(a) shows effective deviation from exact PSC (θ) with Q_{eng} and Q_{true}. Deviation (θ) dropped steeply between Q-factor (Q_{true}) values of 1.15 and 2.5. It then saturated at higher Q values. As indicated in Figures 4(b) and 4(c), the microstructural developments were affected by the Q-factor (Figure 4(b)) and/or θ (Figure 4(c)). Such changes were visualized as grain aspect ratio and in-grain misorientations. The initial equiaxed grain structure had undergone an expected shape change with pilgering. This is best represented with the grain aspect ratio. A grain was defined from the continuous presence of > 5° boundaries. Ratio of grain dimensions $\left(\frac{\text{grain size along ND}}{\text{grain size along PD}}\right)$ was the grain aspect ratio. As shown in Figure 4(b) and 4(c), the aspect ratio appeared to drop between Q values of 1.15 and 1.7, corresponding to θ of 0.88 and 0.93, respectively. Beyond Q = 1.7 (or θ = 0.93), however, Q did not appear to affect the aspect ratio significantly. Interestingly, the trend was similar for in-grain misorientation developments: KAM (kernel average misorientation) and GAM (grain average misorientation). KAM represents the average misorientation between each measurement point and its immediate neighbours: provided such misorientation does not exceed 5°. GAM, on the other hand, represents average point-to-point misorientation inside an EBSD grain. Both KAM and GAM increased between Q values of 1.15 and 1.7 (or θ = 0.93), and then saturated.

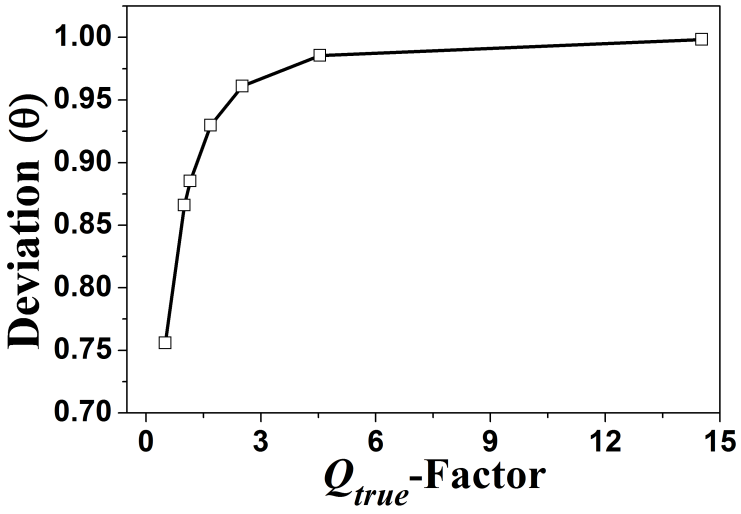

(a)

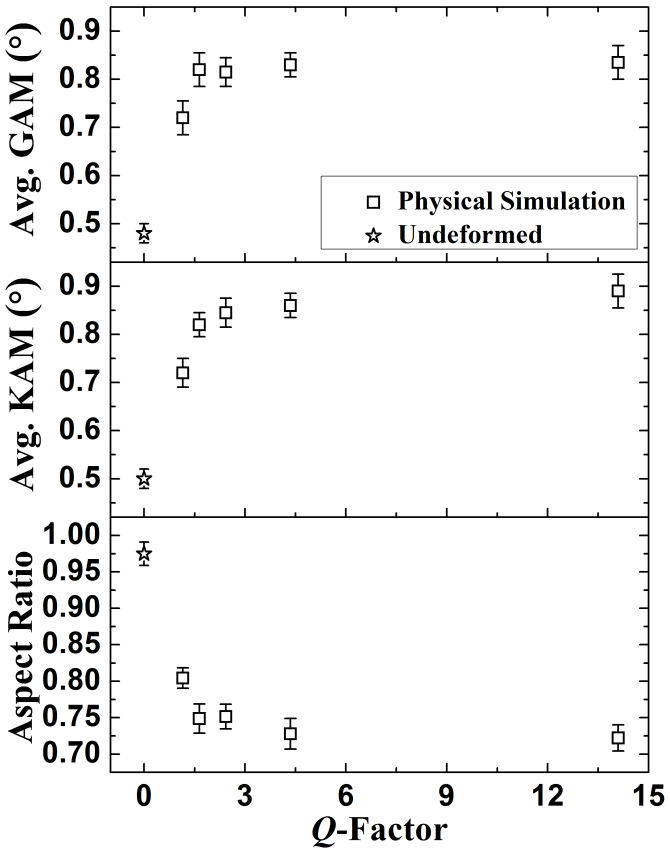

(b)

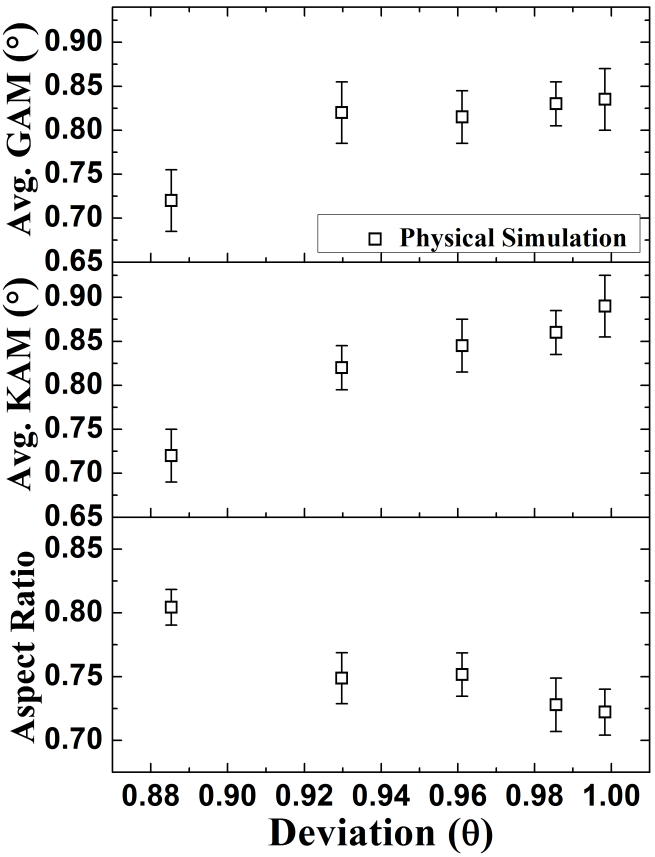

(c)

Figure 4: (a) Effective deviation from PSC (plain strain compression) is quantified by the parameter $\square$ which varies with Q_{true}. Variation of the average grain aspect ratio, KAM (kernel average misorientation) and GAM (grain average misorientation) with (b) Q-factor and (c) Deviation (θ). Error bars indicate standard deviations from multiple EBSD scans.

4.2. Crystallographic Texture

The X-ray orientation distribution functions (ODFs) for the deformed samples are shown in Figure 5. The initial specimen had a non-random texture with well-defined fibers. Figure 5(a) shows $\varphi_2 = 30°$ ODF section of bulk crystallographic texture measured over 80% of the sample area in the long transverse (PD-ND) section, while Figure 5(b) shows the location dependent (near roll, center and near mandrel) texture developments using micro-focus X-ray diffraction. In the $\varphi_2 = 30°$ ODF sections (Figure 5), the $\langle 10\bar{1}0 \rangle$ fiber was described by the three lines $\varphi_1 = 0°, \varphi_1 = 180°, \varphi_1 = 360°$, while the $\langle 0001 \rangle$ fiber corresponds to the line $\varphi = 0°$ given in Krishna et al. (2008). As seen in the figures, pilgering with increasing Q-factors led to strengthening of the $\langle 10\bar{1}0 \rangle$ fibers. Also, a progressive shortening of these fibers toward the basal line $\varphi = 0$ is observed with increasing Q, or θ. Qualitatively, the bulk and micro-focus measurements were similar. The micro-focus measurements, however, showed stronger maximum ODF intensity ($f(g)_{max}$) or higher order of texturing. The latter can be quantitatively estimated as texture index values,

$$\text{Texture Index (TI)} = \int (f(g)^2) dg. \tag{13}$$

It should be noted that texture indices are considered as a more effective representation of relative anisotropy than the more conventional $f(g)_{max}$ values given in Raveendra et al. (2011). Higher texture index in the micro-focus measurements is attributed to the use of area detector. Texture measurements with area detector are known to estimate stronger crystallographic textures, as shown by Basu and Shankar (2015) and also by Gao et al. (2014).

Q*-factor/*θ	ODF ($\varphi_2 = 30°$)
Standard Section	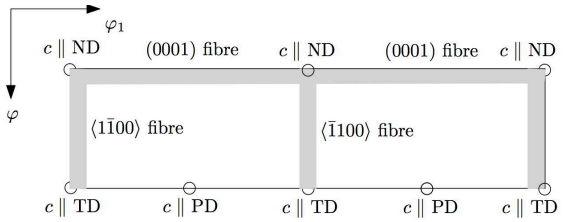
Undef 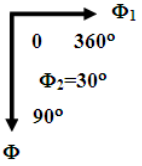	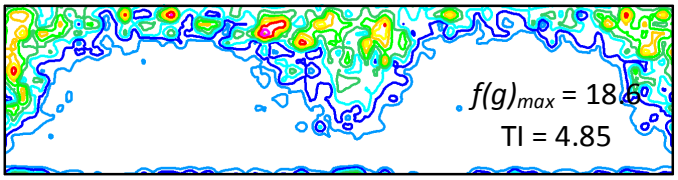
1.15/0.885	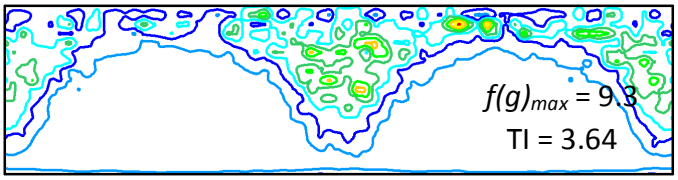
1.69/0.929	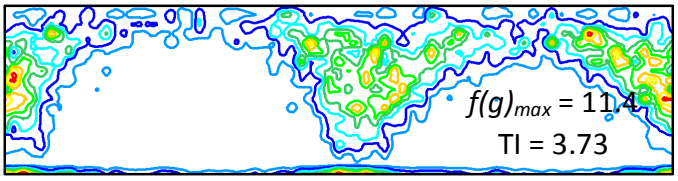
2.51/0.961	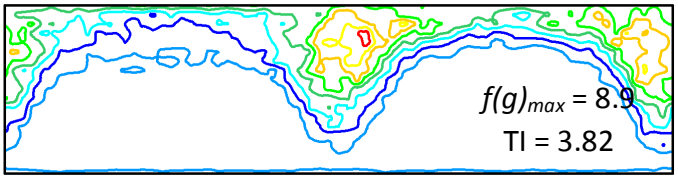
4.54/0.985	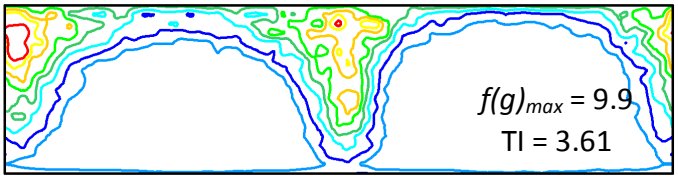
14.5/0.998	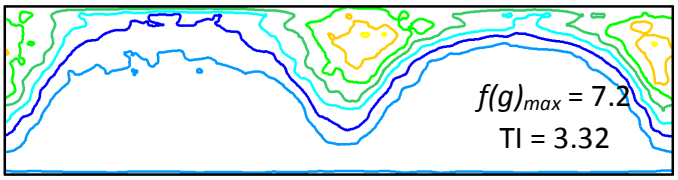

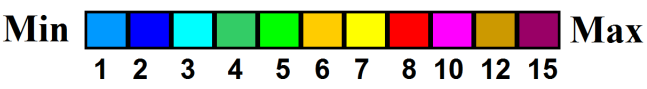

(a)

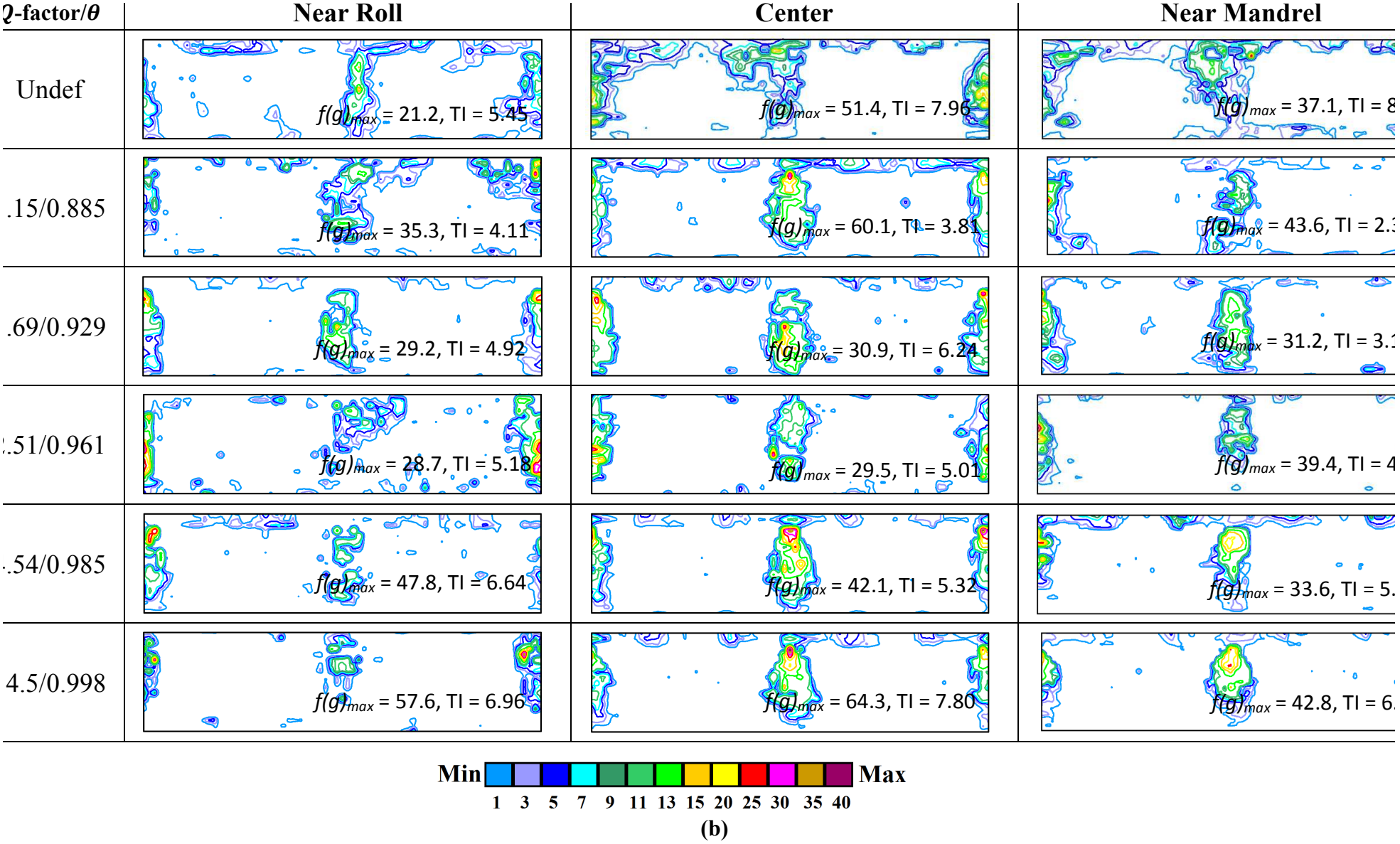

(b)

Figure 5: Experimental ODF ($\varphi_2 = 30$ deg sections) for different Q-factors after simulated pilgering. (a) Bulk measurements over 80% of the sample area and (b) measurements using micro-focus and area detector at different locations: near roll, center and near mandrel. (a) and (b) were measured at respective spot sizes of 800 and 100 microns on the long transverse sections (containing pilgering (PD) and normal (ND) directions) with appropriate oscillations about PD. Maximum ODF intensity and texture index values are given. (a) also includes a standard section with the important/idealized crystallographic fibers.

The Kearns factors, originally proposed by Kearns (1965), are widely used in quantifying crystallographic textures in hexagonal. This is especially relevant to Zirconium, as the nuclear industry has often preferred Kearns factors to more descriptive representations of ODFs. Kearns factors (f) are defined in terms of fractions of grains with their basal poles aligned in a particular direction,

$$f = \int_0^{\pi/2} I_\varphi \sin\varphi \cos^2\varphi d\varphi, \tag{14}$$

where $I_\varphi \sin\varphi$ is the volume fraction of the grains with their *c*-axes oriented at a tilt angle φ from the reference direction, with I_φ expressed in the units of times-random, as detailed by Murty and Charit (2006). For a tube, f measurements are made in the three mutually orthogonal sample directions: axial/pilgering, circumferential, and radial/normal. Figure 6 shows the Kearns parameter estimates from the respective ODFs as functions of the Q-parameter (Figure 6(a)) and θ (Figure 6(b)). The Kearns factors of the undeformed specimen in radial, axial and circumferential directions were 0.48, 0.15 and 0.37 respectively. The Kearns factors (Figure 6) evolved in the same way as the earlier microstructural indices (Figure 5): maximum change till Q of 1.7 (or θ = 0.93), followed by relatively minor modifications. The pilgering physical simulator thus indicated a sharp texture and microstructure evolution till a Q-factor of approximately 1.7. Higher Q-factors did not enforce significant modifications. This itself is not a novel observation. Murty and Charit (2006) and Saibaba (2008) noted a similar saturation with Q-factor. At very low Q-factor, the strain mode is primarily tensile. With higher Q, the strain mode gradually changes to plane strain deformation. The texture and microstructure developments thus depend on the deviation from exact PSC (θ). To test this rationale further, deformation texture simulations were conducted.

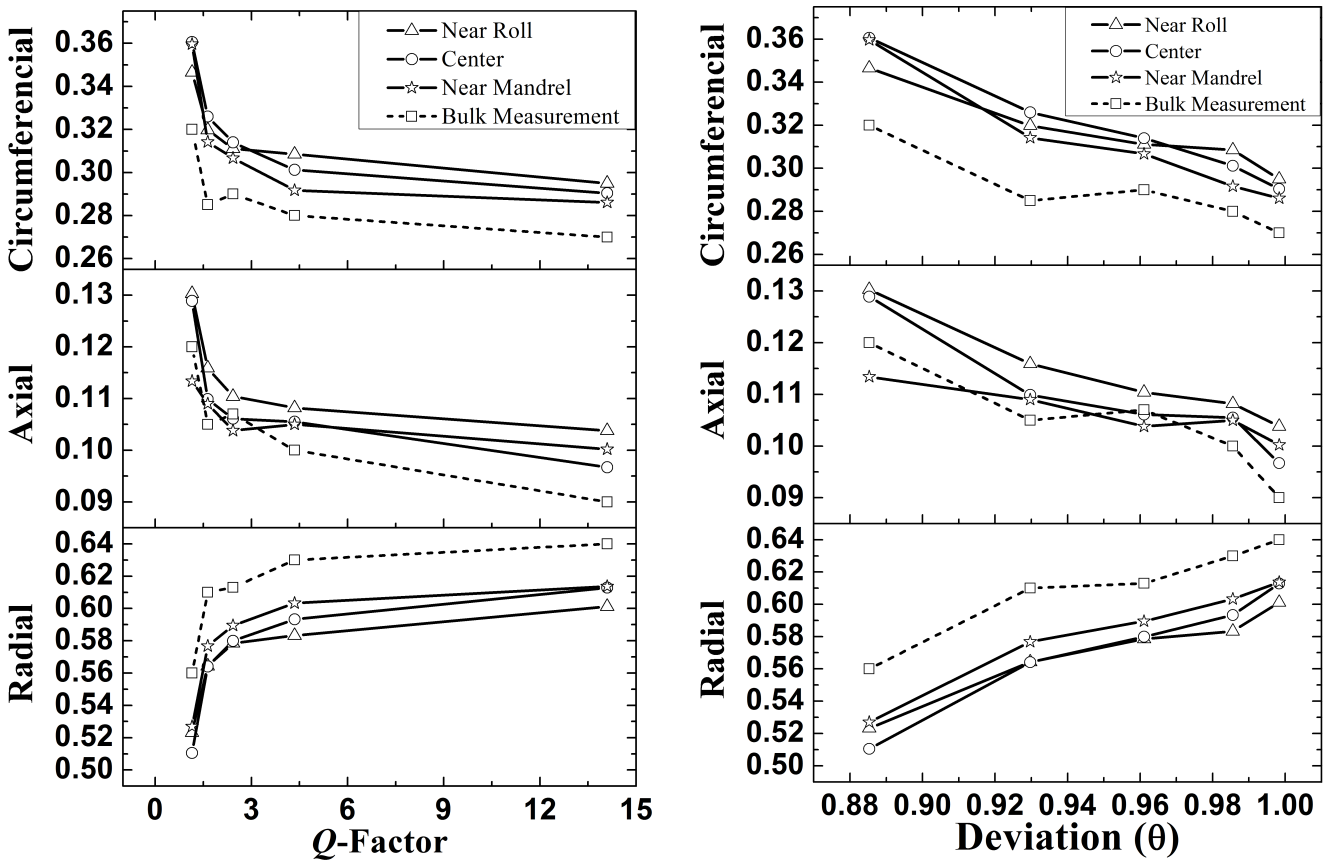

Figure 6: Variation of the circumferential, axial and radial Kearns factors with (a) Q-factors and (b) Deviation (θ). The Kearns factors of the undeformed specimen were, radial: 0.48, axial: 0.15, and circumferential: 0.37. Dashed lines correspond to the bulk texture measurement of Figure 5(a), and solid lines correspond to the micro-focus X-ray measurements of Figure 5(b).

4.3. Computer Simulated Texture

For the deformation texture simulations, flow through a convergent channel (see Figure 1(b) and Eq. (3)) was imposed on a material point. The texture simulations employed the binary tree model described briefly in Sec. 3.3. Further details about this model can be found in Mahesh (2009) and Singh et al. (2015a).

Figure 7(a) shows the $\varphi_2 = 30°$ section of the computer predicted ODFs at the end of the simulated deformation for different Q values. The experimental (bulk measurements) and predicted (texture simulated) Kearns factors are shown in Figure 7(b) (for different Q) and

Figure 7(c) (for different θ), respectively. Kearns factors of the initial (undeformed) specimen used as input in the computer simulations in radial, axial and circumferential directions were 0.53, 0.15 and 0.32 respectively. The corresponding values obtained from the experimental ODF, were 0.48, 0.15 and 0.37. There is a small error introduced already in the initial texture, due to discretization of the continuous ODF.

As shown in Figure 7, simulations were both in qualitative (appearance of the ODFs) and quantitative (Kearns parameter values) agreement with the experimental observations. Figure 7(a) shows that at small values of Q, well developed $\langle 1\bar{1}00\rangle$ and $\langle \bar{1}100\rangle$ fibers develop, which correspond to grains whose basal poles are aligned approximately uniformly transverse to the pilgering direction (Figure 5(a), first row). With increasing Q, however, these grain lattice orientations become biased: the basal poles cluster toward ND and away from TD. These predictions are consistent with the experimental texture measurements shown in Figure 5(a). The quantitative intensity of the computer predicted ODFs is, however, much larger than that of the experimental measurements. This is consistent with previous studies by Lebensohn et al. (1996) and Girard et al. (2001) also, based on the viscoplastic self-consistent model by Lebensohn and Tomé (1993). It appears likely that the prediction of excessive texturing has to do with the imposition of strict compatibility at the model grain boundaries, whereas in the physical material, much localized accommodation of grain boundary incompatibility occurs at grain boundaries shown by Singh et al. (2015b). The qualitative agreement of the predicted and experimentally measured ODFs is reflected in the quantitative agreement between the predicted and experimental Kearns factors in Figure 7(b). The agreement is very good in the axial direction, wherein the discretization error associated with the initial texture was least. In the circumferential and radial directions, the initial texture discretization error (0.05 in the radial direction, and -0.05 in the circumferential direction) is systematically propagated for all values of Q or θ. This suggests that improvements in predicting final Kearns factors can be obtained by using a larger number of discrete grains to describe the initial texture, albeit at greater computational cost. An order of magnitude more grains are required to reduce the discretization error to less than 0.01.

***Q*-factor/θ**	ODF ($\varphi_2 = 30°$)
Undef Φ_1 0 360° Φ_2=30° 90° Φ	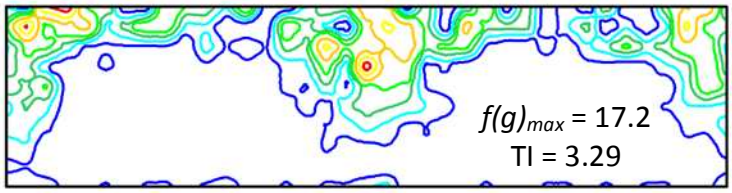
1.15/0.885	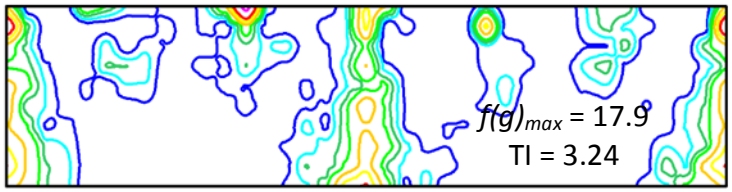
1.69/0.929	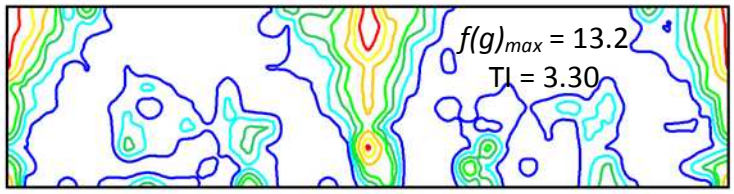
2.51/0.961	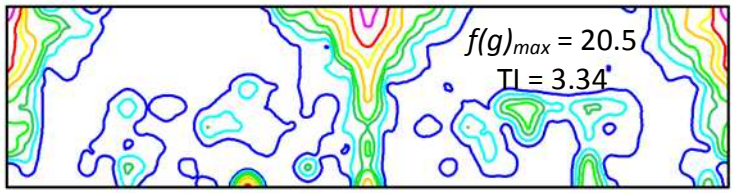
4.54/0.985	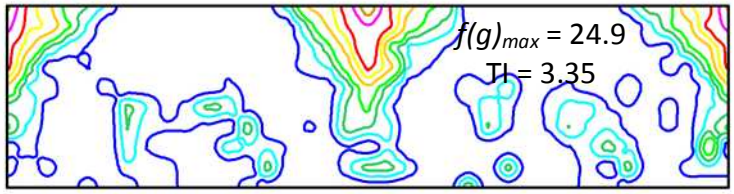
14.5/0.998	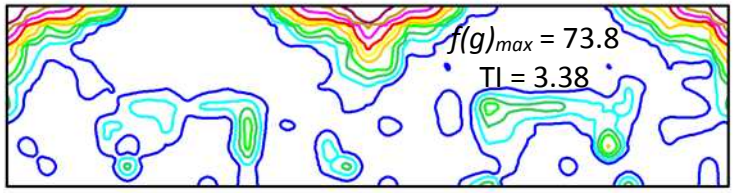

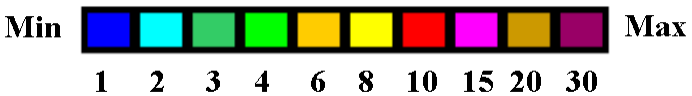

(a)

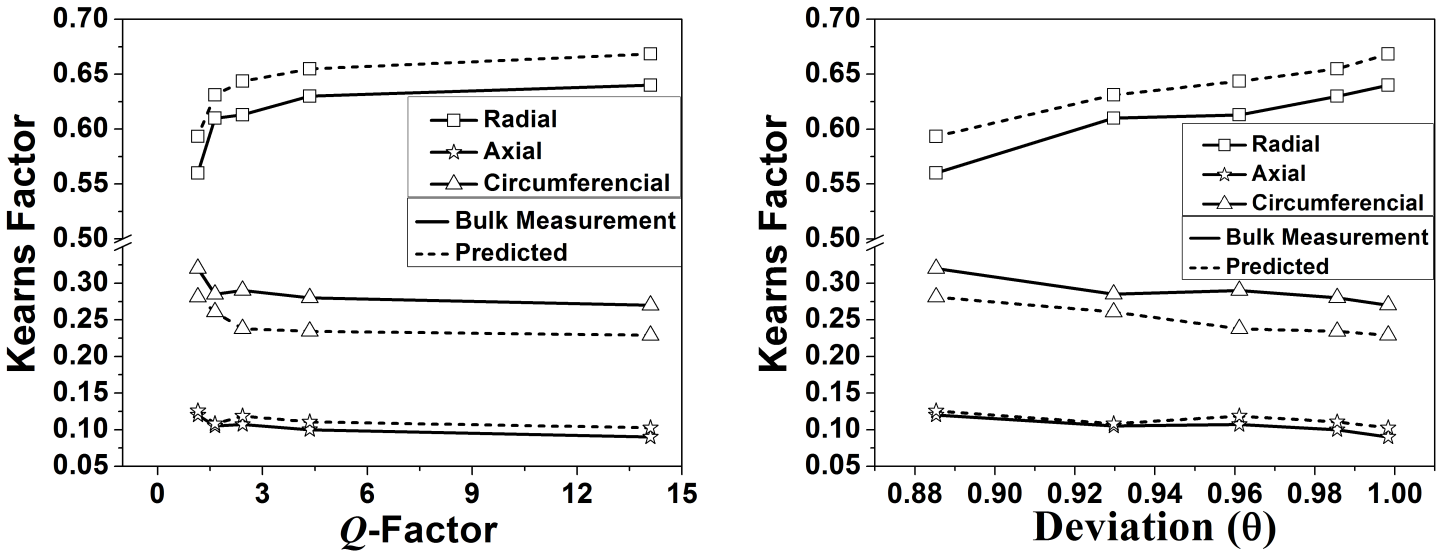

(b) **(c)**

Figure 7: (a) Computer predicted ODF ($\varphi_2 = 30$ deg sections) for different Q-factors. The Kearns factors of the initial (undeformed) specimen used as input in the computer simulations were, radial: 0.53, axial: 0.15, and circumferential: 0.32. Computer predicted Kearns factors are compared with experimentally measurements as a function of (b) Q-factor and (c) Deviation (θ).

It is noteworthy that the present predictions are obtained by imposing a very simple flow field, i.e., flow through the convergent channel, described by the velocity gradient of Eq. (3). Nevertheless, the agreements observed could effectively capture the dependence of the deformation texture development on the Q-factor (and on θ), provided the critical resolved shear stress of the various slip and twinning systems were taken to be those given in Sec. 3.3.

4.4. Texture Asymmetry

Were the present samples to possess monoclinic sample symmetry as given in Randle and Engler (2000), ODF sections shown in Figure 5(a) would be symmetric about the vertical line at $\varphi_1 = 180$ deg. This is clearly not the case. This point is further illustrated by considering the basal pole figures of the final texture inset into Figure 8. A clear bias for the basal poles toward +ND or –ND is observed. As in Singh et al. (2015a), this asymmetry can be quantified by the scalar asymmetry parameter, A, defined as:

$$A = \int_{R} f(\varphi_1, \varphi, \varphi_2)\, dg - \int_{L} f(\varphi_1, \varphi, \varphi_2)\; dg. \tag{15}$$

$f(\varphi_1, \varphi, \varphi_2)$ denotes the orientation distribution function (ODF), and the regions L and R are defined as:

$$R = \{(\varphi_1, \varphi, \varphi_2): 90° \leq \varphi_1 \leq 270°; 0° \leq \varphi \leq 90°; 0° \leq \varphi_2 \leq 60°\}, \text{ and}$$

$$L = \{(\varphi_1, \varphi, \varphi_2): 0° \leq \varphi_1 < 90°; 0° \leq \varphi \leq 90°; 0° \leq \varphi_2 \leq 60°\} \tag{16}$$

$$\cup\ \{(\varphi_1, \varphi, \varphi_2): 270° < \varphi_1 \leq 360°; 0° \leq \varphi \leq 90°; 0° \leq \varphi_2 \leq 60°\}.$$

The volume element dg in orientation space is given by Randle and Engler (2000):

$$dg = \left(\frac{\sin\varphi}{8\pi^2}\right)\, d\varphi_1 d\varphi\, d\varphi_2. \tag{17}$$

The two terms on the right hand side of Eq. (15) are thus the total texture weight near the $\langle 1\bar{1}00\rangle$ fiber and the $\langle \bar{1}100\rangle$ fibers, respectively. The asymmetry parameter A thus quantifies the imbalance in the texture weight of these two fibers. Orthotropic symmetry would imply $A = 0$. The asymmetry parameter, A is discussed in more detail by Singh et al. (2015a).

Figure 8 gives the variation of the asymmetry parameter A with Q and θ. The absolute values of asymmetry parameter A developed in the present simulated pilgering specimen are comparable to that in actual pilgering at the same effective strain, as reported by Singh et al. (2015a). However, the asymmetry parameters deduced from the experimentally measured and computer predicted final textures agree only qualitatively with each other: both show an increasing trend of A with both Q and θ. Quantitatively, the experimental asymmetry parameter A remains positive for all Q and θ, while the predicted value is negative for small Q and approaches the experimental value with increasing Q and θ. Singh et al. (2015a) correlated greater A with a negative frictionally imposed shear strain component, $L_{TD,ND}$. This suggests that the actually imposed flow field on the specimen is one of flow through a convergent channel with a superposed negative $L_{TD,ND}$. Also, the approach of the experimental and computer predicted A toward each other with increasing Q and θ suggests that the frictional lateral shear

component diminishes relative to the normal components as the pilgering deformation approaches plane strain compression, i.e., as $Q \to \infty$ or $\theta \to 1$.

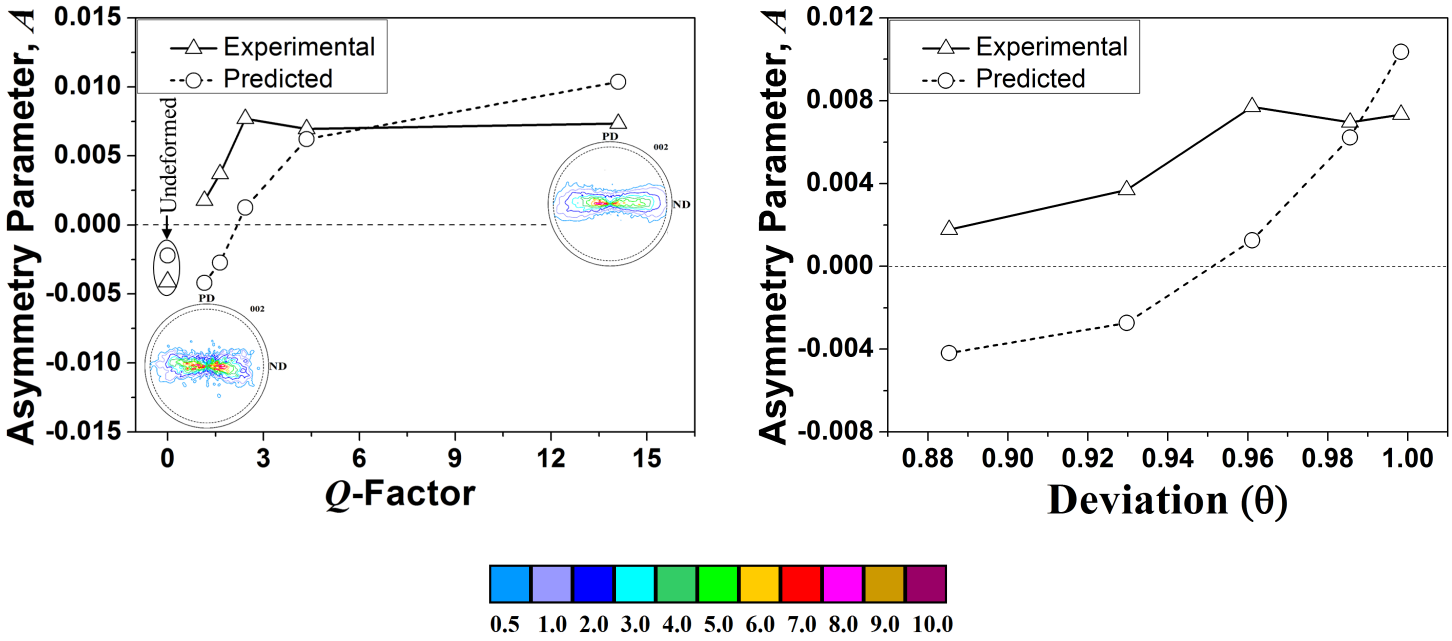

Figure 8: Variation of asymmetry parameter (Singh et al. (2015a)) versus Q-factor and deviation (θ) calculated from experimentally measured ODFs and computer predicted ODFs. The inset pole figures in (a) pertain to the experimental textures indicating the asymmetry present.

5. Discussion and Conclusion

A miniature physical simulator of pilgering was designed and fabricated in this study. The set-up was then used to evaluate the influence of tool geometry, adequately captured by the Q-factor, on the texture/microstructure developments in Zircaloy-4. Texture and microstructure developments quickly saturated with increasing values of Q, and approached the limiting case of plane strain compression in the PD-ND plane. The deviation of the pilgering strain mode from that of plane strain compression, quantified by the scalar parameter θ, mimics the saturation of the texture and microstructure. Polycrystal plasticity simulations are able to qualitatively capture the experimental texture as described by ODFs and quantitatively capture the experimental

Kearns factors. The present work suggests that physical and/or computer simulations can form the basis of a rapid methodology for tool selection to realize desirable post-pilgering textures.

On one hand, computer simulation is unable to quantitatively capture texture development during full-scale pilgering (Singh et al. (2015a)). On the other hand, as shown presently, it is able to do so for physically simulated pilgering. The deformation imposed during simulated pilgering is monotonic. This suggests that the computer simulations adequately account for the micro-mechanisms for accommodating plastic deformation. This leaves imprecise knowledge of the deformation history as the only reason for the observed quantitative deviation in full-scale pilgering. This key insight into the full-scale pilgering process has been made possible by comparing with physically simulated pilgering.

Metal flow, modeled as flow through a convergent channel, in the foregoing modeling works by Lebensohn et al. (1996), Girard et al. (2001), and Singh et al. (2015a) is clearly inadequate as an input for full-scale pilgering simulations. Other approaches, including the finite element-based (Montmitonnet et al. (2002), Lodej et al. (2006)) and analytical (Furugen and Hayashi (1984), Harada et al. (2005)) process models of pilgering offer more realistic deformation histories, but are limited to plastically isotropic materials. The strong texture of the present Zircaloy endows it with a highly anisotropic plastic response. This renders the deformation paths predicted by the aforementioned process models invalid for the present material. To our knowledge, a process model of pilgering incorporating realistic anisotropic plastic response does not presently exist in the literature. Such a model is an essential prerequisite for computationally capturing the full-scale pilgering texture.

A limitation of the physical pilgering simulation is that it does not exactly reproduce the deformation conditions of full-scale pilgering. The imposed deformation in the simulated process is simpler and monotonic, and deviates from that in the full-scale process. This is responsible for the quantitative disagreement between the physically/computationally simulated texture and the full-scale pilgered texture. Three important deviations are listed below.

First, in a full-scale pilgering mill, material points move between the groove and flange regions, and consequently experience shot-to-shot variation in the imposed deformation. On the other hand, since the physical simulator does not involve inserting a draft, or rotating the tube about its axis at the beginning of every shot, a typical tube material point in the pilgering

simulator remains either in the groove or flange (Furugen and Hayashi (1984)) throughout the deformation. This implies that the strain-rate imparted by the full-scale pilgering mill to a typical material point in the tube is highly non-monotonic, while that in the present physical simulator is not.

Second, the friction coefficient between the tooling and work-piece in the present miniature simulator is likely to be significantly larger than that in a full-scale pilgering mill. This is suggested by the observation, in a wide variety of microforming processes, that the friction coefficient increases with specimen miniaturization (Fu and Chan (2013)). These frictional forces will constrain shear deformations in the plane normal to ND, more so in the miniature physical simulator than in the full-scale pilgering mill.

Third, it has been observed that 'biting' of the tube by the rolls at the commencement of every shot in a full-scale pilgering mill produces highly non-homogeneous plastic deformation (Singh et al. (2015a)). This deformation acts to position the tube between the rolls and the mandrel in full-scale pilgering. A corresponding 'biting' step does not occur in either the physical or computational simulation. The simulations will therefore miss the texture evolution that occurs during biting in full-scale pilgering.

Acknowledgments

This research is supported by the Board of Research in Nuclear Science (BRNS) and by the National Facility of Texture and OIM, a DST-IRPHA facility at IIT Bombay, Mumbai, India.

References

Abe, H., Furugen, M., 2012. Method of evaluating workability in cold pilgering. J. Mater. Process. Technol. 212, 1687–1693.

Abe, H., Matsuda, K., Hama, T., Konishi, T., Furugen, M., 1994. Fabrication process of high nodular corrosion-resistant Zircaloy-2 tubing. ASTM Spec. Tech. Publ. 1245, 285–306.

Abe, H., Takeda, L.K., Uehira, A., Anada, H., Furugen, M., 2000. A new fabrication process for Zr-lined Zircaloy-2 tubing. ASTM Spec. Tech. Publ. 1354, 425–459.

Akhiani, H., Szpunar, J.A., 2013. Effect of surface roughness on the texture and oxidation behavior of Zircaloy-4 cladding tube. Appl. Surf. Sci. 285, 832–839.

Allen, V.M., Preuss, M., Robson, J.D., Comstock, R.J., 2005. Evolution of texture in zirconium alloy tubing during processing. Mater. Sci. Forum 495-497, 675–680.

Aubin, J.L., Girard, E., Montmitonnet, P., 1994. Modeling of damage in cold pilgering. ASTM Spec. Tech. Publ. 1245, 245–263.

Basu, S., Shankar, M.R., 2015. Crystallographic textures resulting from severe shear deformation in machining. Metall. Mater. Trans. A 46, 801–812.

Choi, Y., Inoue, H., 2010. Crystallographic texture development and its effect on corrosion behavior of pilgered zirconium alloy tubes. Mater. Trans. 51, 652–658.

Christian, J.W., Mahajan, S., 1995. Deformation twinning. Prog. Mater. Sci. 39, 1–157.

Cullity, B.D., Stock, S.R., 2001. Elements of X-ray Diffraction, 3rd Edition, Prentice Hall. Prentice Hall, New Jersey.

Fu, M.W., Chan, W.L., 2013. A review on the state-of-the-art microforming technologies. Int. J. Adv. Manuf. Technol. 67, 2411–2437.

Furugen, M., Hayashi, C., 1984. Application of the theory of plasticity to the cold pilgering of tubes. J. Mech. Work. Technol. 10, 273–286.

Gao, F., Liu, Z.-Y., Liu, H.-T., Zhang, S.-M., Dong, A.-M., Hao, Y.-S., Wang, G.-D., 2014. Development of γ -fibre recrystallisation texture in medium–chromium ferritic stainless steels. Mater. Sci. Technol. 30, 1735–1741.

Girard, E., Guillen, R., Weisbecker, P., Francois, M., 2001. Effect of plastic shearing on damage and texture on Zircaloy-4 cladding tubes : experimental and numerical study. J. Nucl. Mater. 294, 330–338.

Gurao, N.P., Akhiani, H., Szpunar, J.A., 2014. Pilgering of Zircaloy-4: experiments and simulations. J. Nucl. Mater. 453, 158–168.

Harada, M., Honda, A., Toyoshima, S., 2005. Simulation of cold pilgering process by a generalized plane strain FEM. J. ASTM Int. 2, 1–14.

Hwang, Y.-M., Lin, Y.-K., Chuang, H.-C., 2009. Forming limit diagrams of tubular materials by bulge tests. J. Mater. Process. Technol. 209, 5024–5034.

Kearns, J.J., 1965. Thermal expansion and preferred orientation in Zircaloy. Pittsburgh, PA (USA).

Kocks, U.F., Tomé, C.N., Wenk, H.-R., 1998. Texture and Anisotropy. Cambridge University Press, Cambridge, U.K.

Krishna, K.V.M., Sahoo, S.K., Samajdar, I., Neogy, S., Tewari, R., Srivastava, D., Dey, G.K., Das, G.H., Saibaba, N., Banarjee, S., 2008. Microstructural and textural developments during Zircaloy-4 fuel tube fabrication. J. Nucl. Mater. 383, 78–85.

Krishna, K.V.M., Sain, A., Samajdar, I., Dey, G., Srivastava, D., Neogy, S., Tewari, R., Banerjee, S., 2006. Resistance to hydride formation in zirconium: An emerging possibility. Acta Mater. 54, 4665–4675.

Lebensohn, R.A., Gonzalez, M.I., Tomé, C.N., Pochettino, A.A., 1996. Measurement and prediction of texture development during a rolling sequence of Zircaloy-4 tubes. J. Nucl. Mater. 229, 57–64.

Lebensohn, R.A., Tomé, C.N., 1993. A self-consistent anisotropic approach for the simulation of plastic deformation and texture development of polycrystals: application to zirconium alloys. Acta Met. mater. 41, 2611–2624.

Lodej, B., Niang, K., Montmitonnet, P., Aubin, J.-L., 2006. Accelerated 3D FEM computation of the mechanical history of the metal deformation in cold pilgering of tubes. J. Mater. Process. Technol. 177, 188–191.

Mahesh, S., 2010. A binary-tree based model for rate-independent polycrystals. Int. J. Plast. 26, 42–64.

Mahesh, S., 2009. A hierarchical model for rate-dependent polycrystals. Int. J. Plast. 25, 752–767.

Montmitonnet, P., Loge, R., Hamery, M., Chastel, Y., Doudoux, J.-L., Aubin, J.-L., 2002. 3D elastic-plastic finite element simulation of cold pilgering of zircaloy tubes. J. Mater. Process. Technol. 125-126, 814–820.

Murty, K.L., Charit, I., 2006. Texture development and anisotropic deformation of zircaloys. Prog. Nucl. Energy 48, 325–359.

Peeters, B., Seefeldt, M., Teodosiu, C., Kalidindi, S.R., Van Houtte, P., Aernoudt, E., 2001. Work-hardening/softening behaviour of b.c.c. polycrystals during changing strain paths: I. An integrated model based on substructure and texture evolution, and its prediction of the stress–strain behaviour of an IF steel during two-stage strain paths. Acta Mater. 49, 1607–1619.

Raabe, D., Lücke, K., 1993. Investigation of the ADC method for direct ODF approximation by means of standard functions. Phys. Status Solidi 180, 59–65.

Randle, V., Engler, O., 2000. Introduction to Texture Analysis: Macrotexture , Microtexture and Orientation Mapping. CRC Press.

Raveendra, S., Kanjarla, A.K., Paranjape, H., Mishra, S.K., Mishra, S., Delannay, L., Samajdar, I., Houtte, P., 2011. Strain mode dependence of deformation texture developments: microstructural origin. Metall. Mater. Trans. A 42, 2113–2124.

Saibaba, N., 2008. Fabrication of seamless calandria tubes by cold pilgering route using 3-pass and 2-pass schedules. J. Nucl. Mater. 383, 63–70.

Schmitt, J.H., Aernoudt, E., Baudelet, B., 1985. Yield loci for polycrystalline metals without texture. Mater. Sci. Eng. 75, 13–20.

Shinohara, Y., Abe, H., Iwai, T., Sekimura, N., Kido, T., Yamamoto, H., Taguchi, T., 2009. In situ TEM observation of growth process of zirconium hydride in Zircaloy-4 during hydrogen ion implantation. J. Nucl. Sci. Technol. 46, 564–571.

Singh, J., Mahesh, S., Kumar, G., Pant, P., Srivastava, D., Dey, G.K., Saibaba, N., Samajdar, I., 2015a. Texture development and plastic deformation in a pilgered Zircaloy-4 tube. Metall. Mater. Trans. A 46, 1927–1947.

Singh, J., Mahesh, S., Kumar, G., Pant, P., Srivastava, D., Dey, G.K., Saibaba, N., Samajdar, I., 2015b. Deformation twinning in zirconium: direct experimental observations and polycrystal plasticity predictions. Metall. Mater. Trans. A 46, 5058–5071

Strehlau, O., 2006. Introducing cold pilger mill technology. Tube Pipe J. 1–4.

Tenckhoff, E., 2005. Review of deformation mechanisms, texture, and mechanical anisotropy in zirconium and zirconium base alloys. J. ASTM Int. 2, 1–26.

Tenckhoff, E., 1988. Deformation mechanisms, texture, and anisotropy in zirconium and Zircaloy. ASTM Spec. Tech. Publ. 966, 1–77.

Tomé, C.N., Maudlin, P.J., Lebensohn, R.A., Kaschner, G.C., 2001. Mechanical response of zirconium—I. Derivation of a polycrystal constitutive law and finite element analysis. Acta Mater. 49, 3085–3096.

Vaibhaw, K., Rao, S.V.R., Jha, S.K., Saibaba, N., Jayaraj, R.N., 2008. Texture and hydride orientation relationship of Zircaloy-4 fuel clad tube during its fabrication for pressurized heavy water reactors. J. Nucl. Mater. 383, 71–77.

Van Houtte, P., Li, S., Seefeldt, M., Delannay, L., 2005. Deformation texture prediction: from the Taylor model to the advanced Lamel model. Int. J. Plast. 21, 589–624.

Verlinden, B., Driver, J., Samajdar, I., Doherty, R.D., 2007. Thermo-Mechanical Processing of Metallic Materials. Elsevier (Pergamon Materials Series).

Table 1: Initial and final tube wall thicknesses and diameters of the five specimens studied.

Table 2: Q-factors, final effective strain $(\bar{\varepsilon})$ and deviation (θ) for the five specimens. The Q-factors were calculated as both Q_{eng} (Eq. (1)) and Q_{true} (Eq. (2)), final effective strain $(\bar{\varepsilon})$ (Eq. (11)) and deviation (θ) (Eq. (7)).

Table 3: Chemical composition of Zircaloy-4 used in this study.

Figure 1: Schematic of the (a) pilgering process and (b) flow through a convergent channel. (a) highlights the grooved roll-die and the mandrel: tools important for the physical simulator. (b) was used in an earlier study by Gurao et al. (2014) and Singh et al. (2015a), as well as in the present manuscript, for modeling the texture developments during pilgering. In (b), pilgering (PD) and normal directions (ND) are shown. Also indicated are the initial and final tube diameters (d_0 and d) and wall thicknesses (t_0 and t).

Figure 2: Engineering drawings of the: (a) roll-die and (b) mandrel. Both front and side views are included. All dimensions in mm. Actual photographs of (c) roll-die (plus housing) and (d) mandrel.

Figure 3: Binary tree based model (Mahesh (2009)) of a schematic idealized microstructure. (a) Idealized microstructure; (b) Balanced binary tree representation of (a).

Figure 4: (a) Effective deviation from PSC (plain strain compression) is quantified by the parameter $\square$ which varies with Q_{true}. Variation of the average grain aspect ratio, KAM (kernel average misorientation) and GAM (grain average misorientation) with (b) Q-factor and (c) Deviation (θ). Error bars indicate standard deviations from multiple EBSD scans.

Figure 5: Experimental ODF (**$\varphi_2 = 30$** deg sections) for different Q-factors after simulated pilgering. (a) Bulk measurements over 80% of the sample area and (b) measurements using micro-focus and area detector at different locations: near roll, center and near mandrel. (a) and (b) were measured at respective spot sizes of 800 and 100 microns on the long transverse sections (containing pilgering (PD) and normal (ND) directions) with appropriate oscillations about PD. Maximum ODF intensity and texture index values are given. (a) also includes a standard section with the important/idealized crystallographic fibers.

Figure 6: Variation of the circumferential, axial and radial Kearns factors with (a) Q-factors and (b) Deviation (θ). The Kearns factors of the undeformed specimen were, radial: 0.48, axial: 0.15, and circumferential: 0.37. Dashed lines correspond to the bulk texture measurement of Figure 5(a), and solid lines correspond to the micro-focus X-ray measurements of Figure 5(b).

Figure 7: (a) Computer predicted ODF (**$\varphi_2 = 30$** deg sections) for different Q-factors. The Kearns factors of the initial (undeformed) specimen used as input in the computer simulations were, radial: 0.53, axial: 0.15, and circumferential: 0.32. Computer predicted Kearns factors are compared with experimentally measurements as a function of (b) Q-factor and (c) Deviation (θ).

Figure 8: Variation of asymmetry parameter (Singh et al. (2015a)) versus Q-factor and deviation (θ) calculated from experimentally measured ODFs and computer predicted ODFs. The inset pole figures in (a) pertain to the experimental textures indicating the asymmetry present.